Design of a locally resonant system to reduce noise inside the payload fairing of a launcher during the lift-off

M. Chimeno Manguán, F. Simón Hidalgo, P. Barriuso Feijoo, M.S. Escartí-Guillem, P. Nieto, J.-P. Groby, J. Leng, V. Romero-García

Design of a locally resonant system to reduce noise inside the payload fairing of a launcher during the lift-off

M. Chimeno Manguán[a,*], F. Simón Hidalgo[b], P. Barriuso Feijoo[c], M.S. Escartí-Guillem[c,d], P. Nieto[c], J.-P Groby[e], J. Leng[f], V. Romero-García[d]

[a] *Universidad Politécnica de Madrid, Pza. Cardenal Cisneros, 3, 28040, Madrid (Spain)*
[b] *ITEFI-CSIC, C/ Serrano 144, 28006, Madrid (Spain)*
[c] *Comet Ingeniería, Convento Carmelitas, 2, 46010, Valencia (Spain),*
[d] *Instituto Universitario de Matemática Pura y Aplicada (IUMPA, Universitat Politècnica de València), Camino de Vera s/n, 46022, Valencia (Spain),*
[e] *Laboratoire d'Acoustique de l'Université du Mans (LAUM), UMR CNRS 6613, Institut d'Acoustique - Graduate School (IA-GS), CNRS, Av. Olivier Messiaen, 72000, Le Mans (France),*
[f] *Laboratoire d'Acoustique de l'Université du Mans (LAUM), UMR CNRS 6613, Institut d'Acoustique - Graduate School (IA-GS), CNRS, Av. Olivier Messiaen, 72000, Le Mans (France),*

Abstract

The high sound pressure exerted on the payload during the launch of space vehicles can jeopardize its structural integrity. Given space and weight restrictions, designing fairing noise protection systems is not easy and the number of alternatives is limited, especially for small launchers. This work proposes the design of an acoustic protection based on an simultaneous increase of insulation and absorption in the system tailored to the payload fairing of a space launcher. To this end, the use of a panel made of Helmholtz resonators is investigated. The panel presents a deep subwavelength thickness, as well as a highly efficient acoustic protection (90% of absorption and 13 dB of Transmission Loss) over the frequency range of interest. The panel is designed by considering a reciprocal and non mirror symmetric transmission problem and the acoustic incidence from both sides of the panel. A high Transmission Loss in the frequency range of interest is then obtained when considering an incidence coming from the outside of the payload fairing, whereas the quasi-perfect absorption of acoustic waves is observed in the case where the incidence comes from the inside of the fairing. The panels are subsequently prototyped and their performance is experimentally evaluated. Measurements are correlated and discussed in view of the theoretical and numerical predictions. This mitigation approach sets a new trajectory for innovative noise reduction in small-scale space launchers.

Keywords: Lift-off noise, vibroacoustics, quasi-perfect absorption, noise reduction, Numerical prediction, Hemholtz resonator

*Corresponding author

September 5, 2024

1. Introduction

Since the first launch of the Sputnik launch system in 1957, launchers have dramatically increased their reliability and efficiency in terms of payload capacity, cost-effectiveness, and reusability [1]. However, the detrimental effect induced by the dynamic environment that a satellite endures during its journey to orbit has not changed much over since then. In this context, the vibroacoustic load specification that a spacecraft must be able to withstand is one of the most strict requisites in the design and manufacturing stages [2, 3].

Vibroacoustic loads are generated during lift-off and atmospheric flight of space launchers [4]. Noise levels reached during lift-off are higher than during the flight due to the intense pressure waves generated by the rocket engines [5]. The engine exhaust jet produces a strong, supersonic regime that is reflected from the launch pad towards the launch vehicle, producing acoustic loads on the payload fairing (PLF) [6]. These acoustic loads can then reduce the structural integrity of the PLF and the payload itself.

The payload sent into space usually contains fragile components whose functionality may be affected when subjected to medium or high amplitudes vibrations [2]. In addition, certain structures that are part of almost any payload, such as solar arrays, antennas or panels to support equipment, have high surface-to-thickness ratios, which, together with their increasingly lower density, make them susceptible to a strong vibroacoustic coupling with the driving sound field [7, 8].

Regardless of the strategies that spacecraft manufacturers use to reduce vibroacoustic coupling and improve its structural stability, launch vehicle manufacturers must also develop systems that reduce as much as possible the sound field to which this payload will be subjected. This reduction will result in not only a better integrity of the payload but also can contribute to reduce costs and improve competitiveness [3].

The noise inside the PLF can be reduced in two ways: either by increasing its acoustic insulation or reducing the noise level inside it by using sound absorbent elements [9, 10]. Improving PLF insulation is often ruled out, as structural and weight-reduction aspects often take priority. Nevertheless, the use of structural dampers, sometimes combined with sound absorbers, has been studied [11]. To effectively attenuate the sound field inside the PLF, the integration of sound absorbing elements becomes crucial. The two elements commonly used for sound absorbtion are acoustic blankets and Helmholtz resonators (HRs).

Acoustic blankets are sound proofing devices consisting in a porous material enclosed by fabric that are directly attached to the PLF structure. The sound pressure is dissipated though viscothermal processes when propagating through the blanket. Also, the attachment of the blankets to the PLF increases its vibration damping, which reduces the acoustic transmission through it [12, 13, 14]. Although they usually have low density and thickness, which is a great advantage, their absorption capacity usually increases with density up to a certain threshold while the lower cut-off frequency is proportional to their thickness. The thickness of such systems typically ranges from 2.5 cm to 10 cm and their absorption efficiency is becoming important above 800 Hz. As a result, they are less effective for both attenuating and absorbing the noise at lower frequencies corresponding to the first acoustic modes inside the PLF.

A possible substitute for acoustic blankets are micro-perforated panels [15]. This element consists of a rigid surface whose perforations (typically circular holes or slits) are distributed periodically. The sound attenuation is due to viscous friction and thermal conduction in the inner air of the perforations. These systems can compete with acoustic blankets in terms of weight and space constraints. Their solid materials make them easy to maintain and avoid debris that acoustic blankets generally produce inside the PLF. They can be modelled as an association of resonators sharing the same cavity [16], offering some design flexibility. Micro-perforated panels can be easily integrated into the PLF structure so that no space is lost and minimum mass is added. These solutions can offer almost 6 dB of noise reduction at 400 Hz and about 12 dB at 2 kHz [17].

Acoustic resonators possess a great absorption in their working frequency band, which is usually narrow; resonator configurations can be designed so that the thickness required to work at low frequencies is, contrary to the case of blanckets, much smaller than the wavelength of the working frequency, i.e., they are deep subwavelength. These characteristics make them a good option for the attenuation of the main modes inside the fairing [18, 19, 20]. The incorporation of these acoustic resonators within the core of the fairing structure prevents the loss of useful cargo volume [21, 22, 23]. The association of resonators tuned at different frequencies makes it possible to widen the working bandwidth of the absorbing element [24, 25]. Optimisation algorithms also help to improve the performance of resonator assemblies or solutions combining resonators and acoustic blankets [26].

The acoustic field inside the PLF depends on the payload and its spatial distribution within the fairing. One attenuation strategy that can take this aspect into account and be adapted to any launch configuration is using active noise control systems. The controls can be carried out in the structural [27, 28] or acoustic field [29]. However, active noise control systems require more space and mass addition than passive ones. Their implementation is moreover much more complex. They are therefore not currently considered to be an effective mitigation solution for aerospace applications.

In the last decade, new techniques for designing resonators have emerged. These techniques showed that the perfect absorption of an incident acoustic wave can be reached with resonators by balancing the energy leakage from the resonators with their intrinsic losses at the resonant frequencies. [30, 31, 32]. In the case of transmission problems, two possibilities can be used: *i*) non mirror detuned arrays of resonators [33, 34, 35] or *ii*) degenerate resonators [36, 37]. In both cases, the critical coupling condition ensures the balance between the energy leakage and the intrinsic losses of the resonator.

In this work, a noise control treatment for a fairing based on resonators with mquasi-perfect absorption has been designed. The design techniques used allow the calculation of the acoustic transmission through the PLF and have been combined with optimisation algorithms for the best treatment design. The prototype is designed to be attached to the inner side of the fairing shell. In this way, resonators with a double use (inner sound absorption and insulation) are developed and a solution is obtained that makes the most of the performances of this type of device. The optimisation process also considers the thickness of the solution so that the resulting resonator will take up as little space (thickness) as possible inside the fairing.

The level of noise reduction offered by the solution under use conditions can only be determined experimentally by testing the real configuration. Instead, the performance of the solution has been estimated using a numerical model that accounts for the two contributions to noise reduction (transmission loss and sound absorption) and by measuring the performance of panel of resonators of reduced size.

2. Case study

The reduction of the acoustic load inside the payload fairing of the VEGA rocket [5] is addressed. The payload fairing is manufactured by Beyond Gravity and has a diameter of 2.60 m and a height of 7.88 m [5]. During lift-off, the payload is subject to acoustic loads due to the engine plume impingement on the launch pad as seen in Fig. 1. The envelope spectrum of Sound Pressure Level (SPL) inside the fairing for lift-off is shown in Table 1.

This case was analysed under a European Space Agency (ESA) program to develop a sound reduction system applicable to the VEGA rocket. Based on information provided by ESA, Figure 2 shows the acoustic insulation computed as the difference between the mean value of the measurements by external microphones and the mean value of the measurements by the internal microphones. It is shown in dB relative to its minimum and the dimensionless frequency f/f_t where

Figure 1: VEGA launch picture taken on 2018 in Kourou.

Table 1: Acoustic noise spectrum under the VEGA fairing during lift-off in octave bands and the overall SPL value [5]

Octave band (Hz)	SPL (dB)
31.5	112
63	123
125	126
250	135
500	138
1000	127
2000	120
OASPL	140.3

f_t is the frequency for minimum insulation and it is therefore the target frequency for the design of the acoustic solution. This value is the target frequency for the design of the quasi-perfect absorption solution.

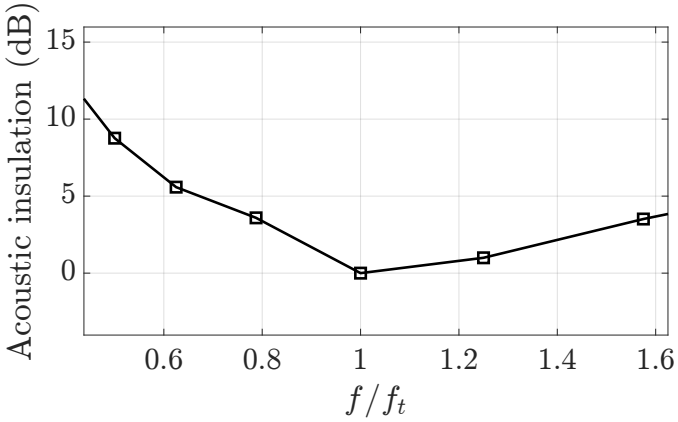

Figure 2: VEGA fairing acoustic insulation determined from flight measurements

3. Design of the resonator

In this work, the acoustic protection of the fairing is operated by an array of HRs embedded in a panel that can be attached to the fairing. The HR is designed in such a way that the panel presents a quasi-perfect absorption at the target frequency f_t.

Given that there is only one target frequency and the small diameter of the launcher considered, a single resonator design is considered. The HR panel is then made up of identical HRs with a thickness of 1 cm. For the design, both acoustic transmission and absorption are taken into account. The studied structure, therefore, is formed by the fairing sandwich plate (Fig. 3a) and, attached to it, a set of resonators connected to the interior cavity by a slit as shown in Fig. 3b.

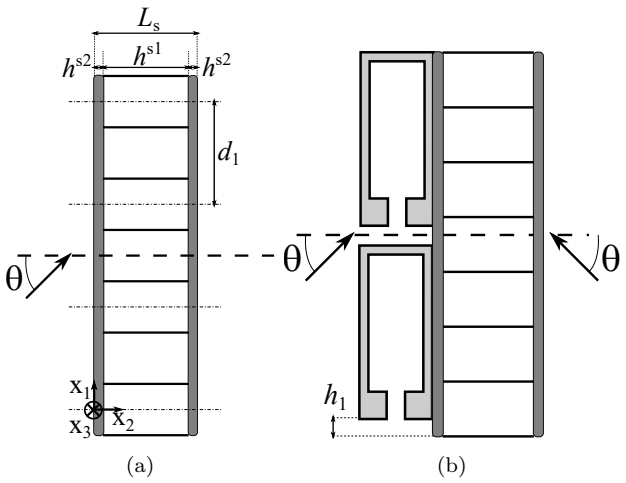

Figure 3: (a) fairing shell structure, (b) HR panel plus fairing.

3.1. Vibro-acoustic modelling

The sound transmission through the fairing structure is modelled using the Transfer Matrix Method (TMM) [31, 38, 39]. The material assumes an infinite length along the x_1 direction, with different properties in the (x_2, x_3) plane (see Fig.3a). Since the solid properties remain the same along the x_1 direction, it is possible to consider it as a periodic repetition of a unit cell of length d_1 along this direction. This assumption allows to decompose all the quantities in the solid

into Bloch waves and then account for the coupling between the structure and the HR panel.

The geometry considered in the system allows considering plane wave propagation [40]. In this way, the sound pressure and normal acoustic flow velocity on both sides of the system are related using TMM. The change in the different cross-sections is considered by including radiation correction lengths. The visco-thermal losses of the air filling each HR and slit are also taken into account by considering complex, frequency-dependent density and bulk modulus [41].The resonant panel is described as an equivalent fluid system and the vibroacoustic coupling between the panel and the fairing structure is ensured by considering the continuity of the normal velocity between both systems. Details of the analytical model can be found in Appendix A. This vibroacoustic problem allows considering any incidence angle, so diffuse scattering coefficients can be calculated.

3.2. Optimisation method

In order to obtain a quasi-perfect absorption at f_t by the resonant panel, the analytical model described in Sec. 3.1 is combined with an optimisation algorithm applied to the resonator geometry.

The scattering properties of the complete system, including the fairing sandwich structure and the HR panel, depend on the geometrical parameters of the resonator panel. To find the best configuration for the target frequency, an optimisation method is used. Sequential Quadratic Programming (SQP) [42] is used in Matlab [43]. A single resonator is considered whose geometry is depicted in Figure 4. The resonators panel thickness is fixed to $w_{c2} = 1$ cm to ensure a thin noise reduction solution compatible with the fairing reduced space availability.

Therefore, the input parameters are limited to the geometric dimensions of the resonator in the (x_1, x_3) plane. The optimization problem is carried out assuming a diffuse field at the target angular frequency $\omega_t = 2\pi f_t$ where all possible incidence angles are taken into account. In this case

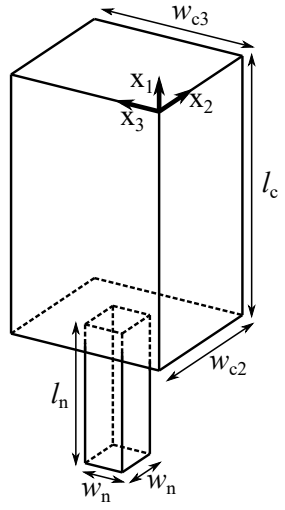

Figure 4: Geometry of the HR considered for the optimisation

the cost function is

$$e(h_1, h_3, w_n, l_n, w_{c,2}, w_{c,3}, l_c) = \\ = 1 - \frac{\int_{\theta=0}^{\pi/2} \alpha^-(\omega_t, \theta) \sin(\theta)\cos(\theta) d\theta}{\int_{\theta=0}^{\pi/2} \sin(\theta)\cos(\theta) d\theta} \quad (1)$$

where θ is the incidence angle and α^- the absorption coefficient if we consider an incidence from the side of the resonant panel. $\alpha^-(\omega_t, \theta)$ is calculated by using the analytical model described in the Appendix A.

The acoustic coefficients of the optimised design are shown in Fig. 5. The absorption coefficient is maximum at $0.99 f_t$ with a value of 0.94 for normal incidence and 0.96 for diffuse field. The Transmission Loss maxima are slightly shifted to higher frequencies with maximum values of 171 dB at $1.05 f_t$ for normal incidence and 166 dB at $1.03 f_t$ for diffuse field. Note that a typical porous material analyzed under the assumptions of the Delany-Bazely model with the same thickness and a flow resistivity value of 80 kPa·s·m^{-2} would have an absorption coefficient value of about 0.12 at the working frequency at it will be mostly transparent to sound.

3.3. Experimental validation

To determine experimentally the absorption and reflection coefficients of the resonator an HR

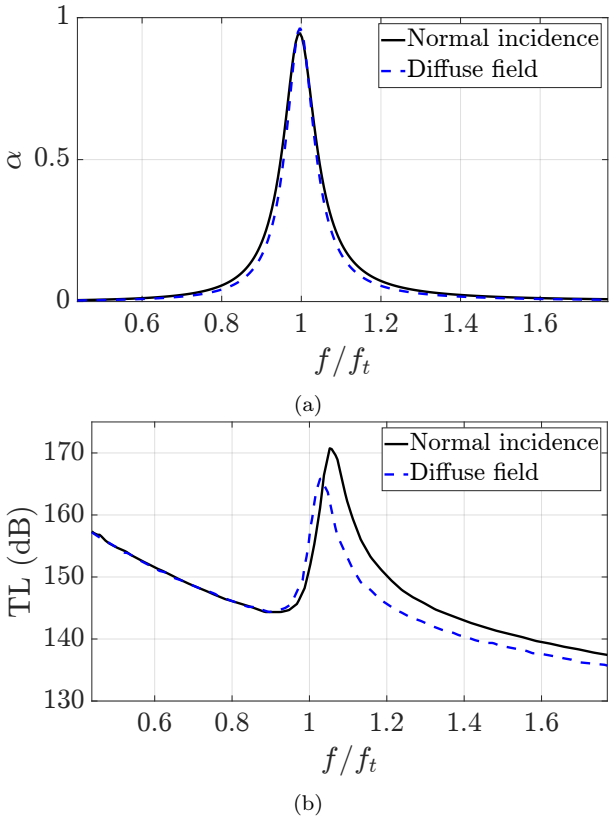

Figure 5: Analytical a) absorption coefficient and b) Transmission Loss in normal incidence (black solid line) and diffuse field (blue dotted line)

panel is manufactured and tested in an impedance tube. The panel was made by additive manufacturing using a ProX SLA printer with Accura 60 due to its low surface roughness properties compared to other 3D printing techniques such as Fused Filament Fabrication or Fused Deposition Modelling. The Computer-Aided Design (CAD) of this panel and the fabricated sample are depicted in Fig. 6.

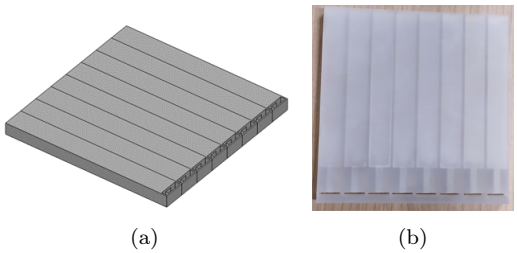

Figure 6: HR panel sample for measuring the absorption and reflection coefficients in an impedance tube: (a) CAD design. (b) actual panel

The absorption and reflection coefficients are measured in an impedance tube with an anechoic termination for frequency below the cut-off frequency, that is 2.75 times the target frequency f_t, ensuring the plane wave assumption around the target frequency. The test was carried out for several overall levels from 103 dB to 120 dB with the absorption curves showing negligible differences with the same trend expected for higher values.

Two pairs of calibrated G.R.A.S. microphones, one on each side of the sample, was used to measure the pressure levels for a 100 dB swept sine load over the frequency range of $0.25f_t - 5f_t$. The comparison between the experimental and the numerical results is shown in Fig. 7.

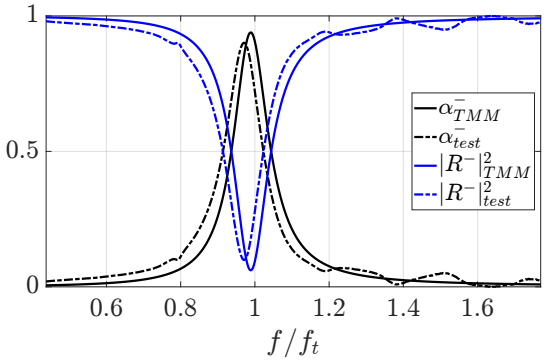

Figure 7: HR panel absorption and reflection coefficients as determined by the analytical model and measured in the impedance tube

4. Numerical model

4.1. Numerical model of the PLF

Two numerical models are used for the vibroacoustic analysis of the VEGA PLF. For the frequency range of interest (centred in f_t), Boundary Element and Finite Element models (BEM and FEM) [44, 45] are developed in VAOne [46]. The external acoustic domain is simulated with an unbounded BEM domain including the acoustic load composed of a set of fifty plane waves distributed evenly in the space and with different incidence angles. The internal acoustic domain is modelled by means of a FEM domain with 687955 three-dimensional elements, depicted in Fig. 8b.

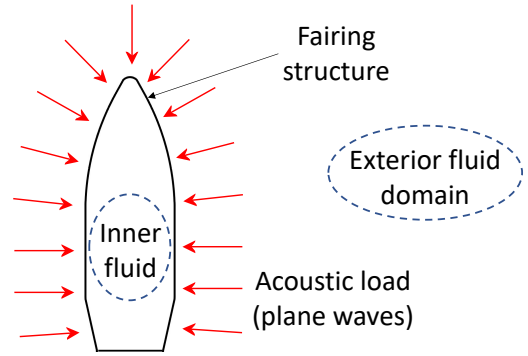

(a) Sketch of the fairing vibroacoustic model

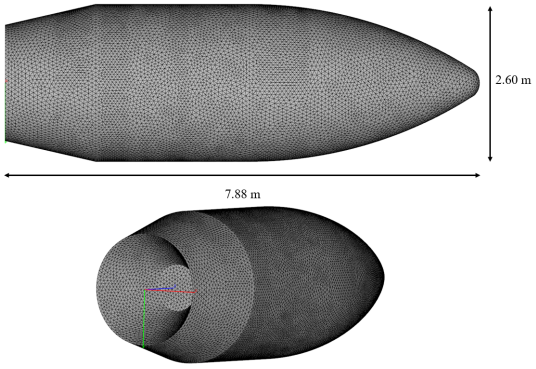

(b) Inner FEM acoustic domain mesh

Figure 8: Details of the fairing vibroacoustic model

The fairing structure is modelled by means of 86556 two-dimensional elements with a simplified structural definition. The total mass and thickness of the PLF structure are approximately 400 kg and 20 mm, respectively. The structure is also considered to be a sandwich panel comprising a 16 mm thick HexWeb® CR III 1/8-5056-.002 honeycomb core between two 2 mm thick CFRP skins composed of M55J. Damping frequency laws are used considering the experimental data available to ensure that the results obtained by the model resemble the actual measurements.

Results for the relative SPL on the external and internal microphone locations are shown in Fig. 9 to show the consistency between the numerical model and the fairing lift-off measurements. Moreover, a comparison of the experimental and the numerical fairing acoustic insulation is depicted in Fig. 10. It can be seen that, the numerical models developed capture the trend of the magnitudes and match the experimental results at the target frequency f_t. The good agreement assures that the numerical models developed are adequate for assessing the quasi-perfect absorption solution for the actual fairing at this frequency.

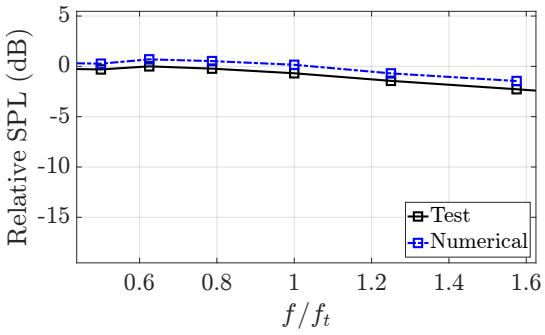

(a) Outside fairing

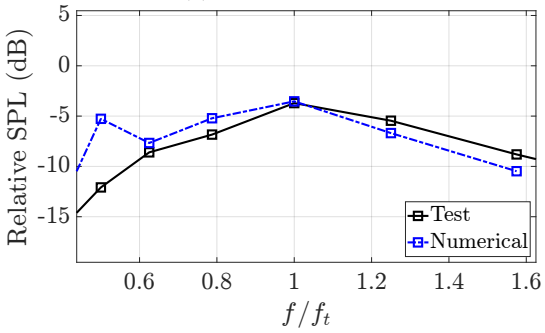

(b) Inside fairing

Figure 9: Test and numerical comparison: (a) Surface SPL outside the fairing. (b) Surface SPL inside the fairing.

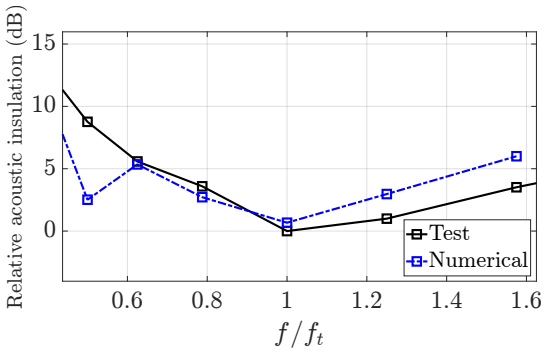

Figure 10: VEGA fairing acoustic isolation determined experimentally and numerically

4.2. Implementation of the mitigation solution

The effect of the resonator proposed has been simulated by means of a simplified system with equivalent structural and acoustic behaviour. More information regarding the methodology to develop a medium with equivalent structural and

acoustic behaviour for the HR panel is explained in [47]. The mechanical behaviour is modelled by a FEM plate using anisotropic elastic equivalent parameters. These parameters are used to define a flat plate whose most relevant eigenfrequencies are tuned to match the relevant eigenfrequencies of the detailed model.

For the acoustic behavior a VAOne Area Isolator 2x2 [46] is inserted between the fairing structure and the internal FEM cavity. This element is a locally reacting impedance model relating the acoustic pressure and velocity on both sides of an element at a given location (i.e., the HR panel). The acoustic impedance matrix of the system is obtained directly from the results of the acoustic design. The area isolator is defined from the Z_{11}, Z_{12}, Z_{21} and Z_{22} such as

$$\left\{ \begin{array}{c} p_s \\ p_f \end{array} \right\} = \left[\begin{array}{cc} Z_{11} & Z_{12} \\ Z_{21} & Z_{22} \end{array} \right] \left\{ \begin{array}{c} v_s \\ v_f \end{array} \right\} \qquad (2)$$

where p_s and p_f are the pressures on the HR panel face next to the fairing structure and on the opposite one in contact with the internal fluid, respectively, and v_s and v_f are the corresponding velocities. Therefore, the impedance boundary condition can model the transmission coefficient and the absorption coefficient as the system has intrinsic losses.

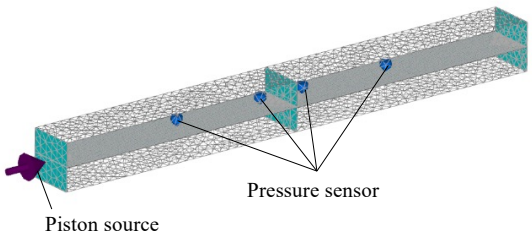

Figure 11: Impedance tube modelled by two FEM fluids, one on each side of the analysed sample.

To validate the 2x2 Area Isolator as an interaction element between a FEM structural domain and a FEM acoustic domain, the impedance tube is modelled by means of two FE acoustic cavities separated by a structural element as depicted in Fig. 11. Two pressure sensors are included on each side to apply the Two Microphone Method. Additionally, a further structural element is included at the left end of the tube, which only has rigid body modes in the frequency analysis range. This element is excited by a point force in the direction of the impedance tube to serve as the system load.

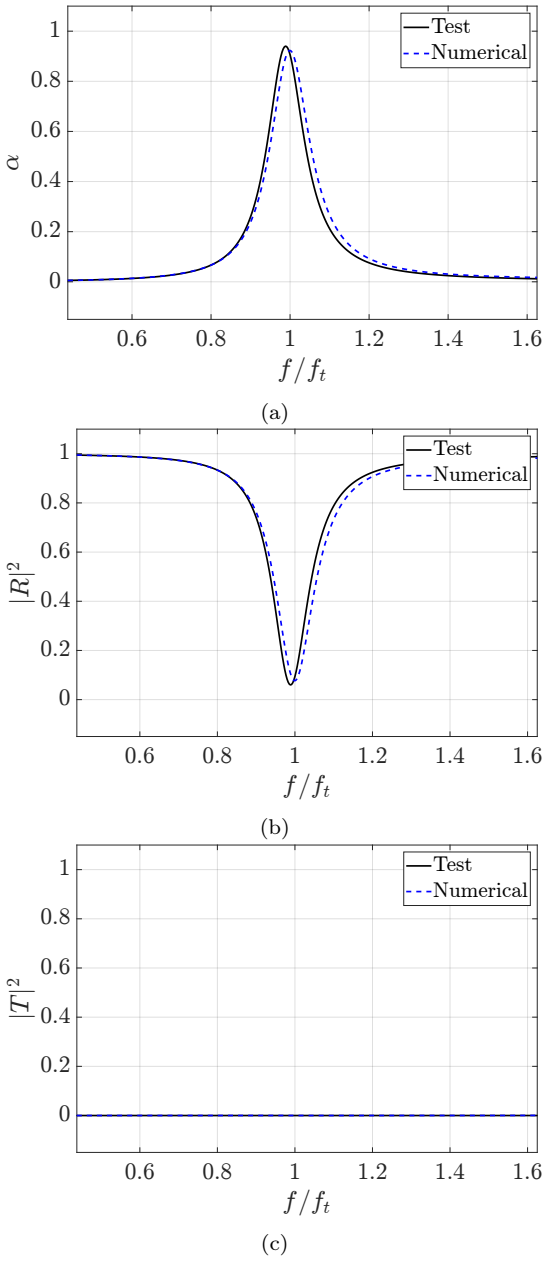

Figure 12: Test and numerical comparison acoustic coefficients: (a) Absorption. (b) Reflection. (c) Transmission.

Figure 12 shows the absorption, reflection and transmission coefficients compared to the analytical values. The numerical simulation of the FEM impedance tube yields highly accurate results for the absorption and reflection coefficient. The results indicate that the FEM model for the interior

acoustic domain, coupled with the 2x2 area isolator to account for the acoustic characteristics of the HR panel, is valid to represent the resonators in the fairing model.

4.3. Target parameters

Acoustic loads inside the PLF determine the environmental load requirements for payloads. Therefore, the acoustic load inside the fairing volume is the target parameter since it represents the acoustic field that payloads must endure. Two quantities are considered: a) the mean average of the SPL at a longitudinal path (parallel to the launcher axis) located at 0.4 m from the fairing centre (Fig. 13), and b) the mean average of the SPL in the whole fairing volume.

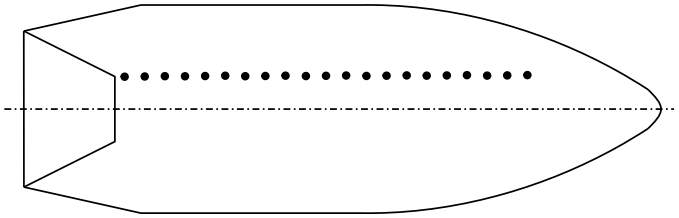

Figure 13: SPL location, black solid circles, for the analysis of the acoustic field close to the payload

The mean SPL along the longitudinal path is of interest since it is placed alongside the usual location of payloads in the fairing, that are installed in the payload adapter. This work assumes an empty fairing so conclusions obtained can be considered independent of the payload (it must be kept in mind that every payload configuration within the PLF will produce a different acoustic field distribution). Therefore, the mean SPL of the whole volume is studied as an estimator of the overall acoustic performances of the solution and the axial values an indicator of space variabilities.

The performance of the noise reduction system will be assessed by comparing these two parameters between the reference fairing and the fairing with the noise reduction system.

5. Results & Discussion

This section presents numerical results of three different models. The first model considers the fairing structure as derived from the available information that resembles the actual fairing insulation (see Fig. 10), that is set as reference. The second model includes the noise reduction system on the whole internal face. This model takes only into account the mechanical behaviour with anisotropic elastic equivalent properties (see Sec. 4.2). The third model includes both the mechanical and acoustic behaviour of the HR panel.

The fairing surface is assumed to be fully covered by the HR panel to provide an upper limit to the effect of the noise reduction system on the acoustic field inside the fairing. The sound pressure levels in the whole volume of the fairing are computed for the three models in 1/24th-octave bands and in 1/3rd-octave bands.

5.1. Longitudinal path

The relative mean SPL along the longitudinal path is depicted in Fig. 14 for the three models.

Figure 14 shows that the structural modification of the fairing structure due to the addition of the HR panel reduces notably the SPL at low frequencies and it has a lesser impact at higher frequencies. In particular, the SPL is reduced by 4 dB in the 1/3rd-octave band centred in f_t.

The effect of the acoustic performance of the resonators leads to a decrease of SPL close to the target frequency, reaching 26 dB at $1.05f_t$ in narrow band and 13.1 dB at the 1/3rd-octave band centred in f_t. This SPL attenuation is also observed at the next 1/3rd-octave band, where the HR absorption is still significant. The frequency for the minimum SPL value matches the frequency for the maximum Transmission Loss from the analytical model (Section 3.2).

5.2. Volume mean

As stated in Section 4.3, the mean SPL of the whole fairing volume is used to assess the acoustic performance of the noise reduction solution.

The mean SPL inside the fairing is calculated for the three models. Results in narrow bands (1/24th-octave bands) and wide bands (1/3rd-octave bands) are depicted in Figure 15.The mean SPL of the reference model (black solid line)

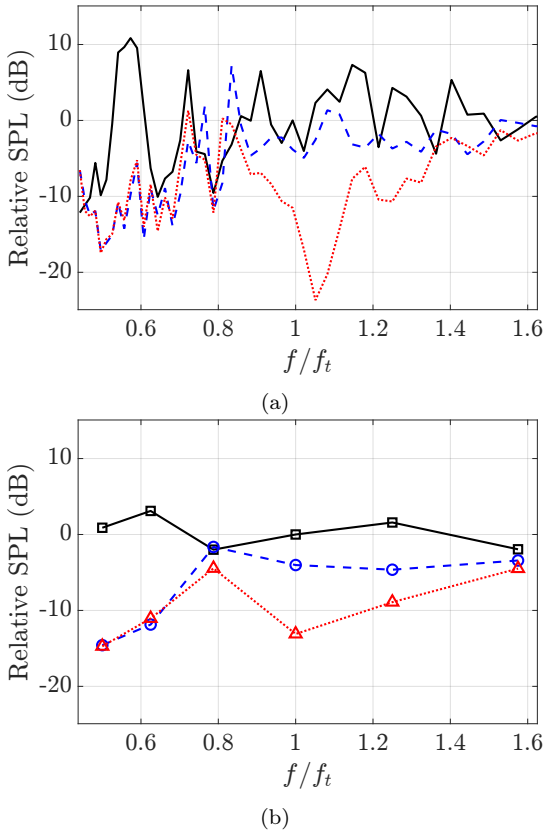

Figure 14: SPL at the longitudinal path of the fairing for the reference model (black solid), and the model including the mechanical behaviour of the noise reduction panel (blue dashed) and the model including both mechanical and acoustic behaviour (red dotted): (a) in 1/24th-octave bands. (b) in 1/3rd-octave bands.

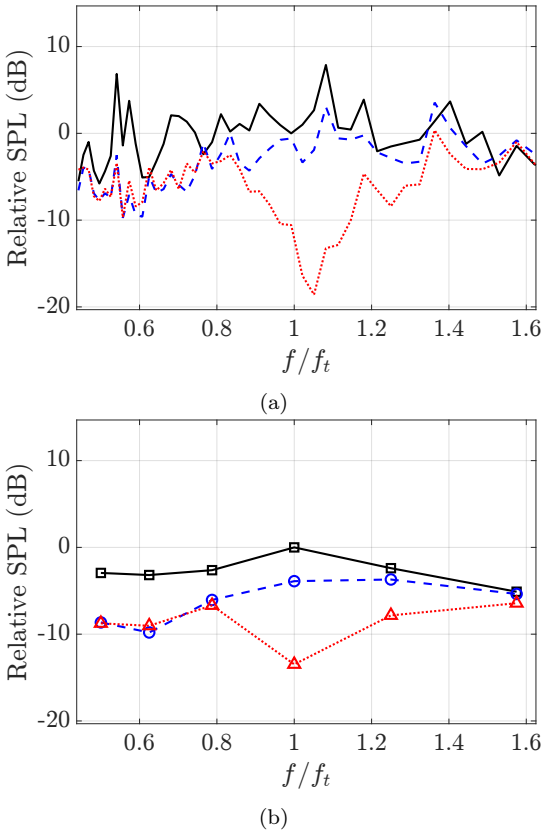

Figure 15: Mean SPL inside the fairing for the reference model (black solid, and the model including the mechanical behaviour of the noise reduction panel (blue dashed) and the model including both mechanical and acoustic behaviour (red dotted): (a) in 1/24th-octave bands. (b) in 1/3rd-octave bands.

shows a maximum at the the target frequency, as it corresponds to the maximum SPL value as expected from the acoustic isolation results in Fig. 10.

As for the SPL at the longitudinal path (Fig. 14), results for the whole volume mean (Fig. 15) show that the structural modification of the fairing structure modifies the acoustic field mainly at low frequencies while the acoustic contribution of HR panel contributes to the attenuation around f_t. In particular, at $1.05f_t$the relative SPL is decreased by 4.6 dB due to the structural contribution of the panel, and by 16.7 dB due to the acoustic one. In the case where the relative SPL is represented in 1/3rd-octave bands, the decreases are 3.9 dB and 13.5 dB, respectively.

The results of the mean SPL of the whole fairing volume are shown in Fig. 15. This value is considered as a better estimation of the effect of the noise reduction system as it takes into account the whole acoustic field and not a given location. Figure 15 shows that the main frequency range of attenuation is located around the target frequency and that a large attenuation of the SPL can be obtained with the proposed design, with up to 13 dB in one-third octave bands. This is an upper limit as the HR panel cannot cover the whole PLF surface in an actual implementation. This is due to the fact that the PLF structure also comprises joint elements and ventilation holes that cannot be obstructed. The curvature of the fairing structure also increases at the top section, making the manufacturing and installation of the resonant structure more intricate.

5.3. Acoustic mitigation on VEGA acoustic spectrum

To illustrate the acoustic effect of the resonators, the approximation of the SPL inside the VEGA fairing during lift-off with and without the resonators is compared. Figure 16 shows in solid red line the lift-off noise spectrum under the fairing as presented in Tab. 1, while the dashed black line represents the spectrum when the solution is implemented on the fairing.

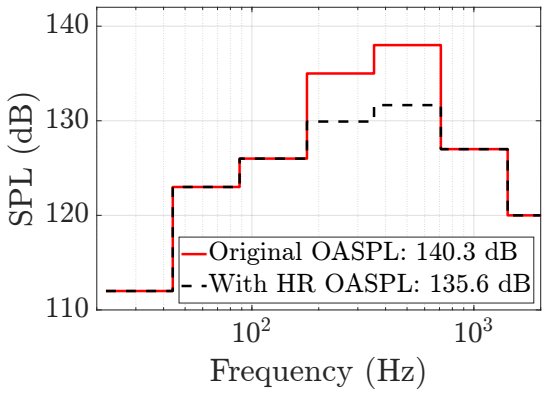

Figure 16: Expected SPL during lift-off with and without the designed solution.

The incorporation of the HR panel produces a noticeable reduction in acoustic loads within the 250 Hz and 500 Hz 1/3rd-octave bands, representing the most significant levels. Consequently, while the HR design targeted optimal performance at a certain frequency f_t, this mitigation effect also extends its influence to adjacent frequencies. Finally, the use ot the HR panel gives an overall SPL reduction of 4.7 dB.

6. Conclusions

This work proposes a noise reduction system based on waveguides loaded by HR as an efficient and reduced-volume solution for rocket PLFs. The system is applied to the Arianespace VEGA rocket and takes into account experimental results on the fairing acoustic isolation. The results show a clear minimum at a single frequency band. A single HR design is obtained by numerical optimization to maximize the acoustic absorption at a target frequency. Numerical and experimental results on an impedance tube show a good agreement. The maximum absorption coefficient is found at the expected frequency but the maximum TL is shifted to slightly higher frequencies. Numerical results on a representative FEM/BEM model of the VEGA fairing show that at the frequency of maximum TL noticeable reduction of the SPL is obtained, up to 13 dB (in 1/3rd-octave bands) for a configuration of full coverage of the fairing internal surface. The actual improvement is expected to be lower since some of the fairing surface is not available for installing the noise reduction system.

Acknowledgments

The authors would like to thank the European Space Agency and in particular the Technology Research Program (TRP) for supporting and granting this work under contract 4000126316/19/NL/LvH of project RED-LAUNCH: Launch Sound Level Reduction and thank Mr Ivan C.S. Ngan (ESA) for his support and fruitful discussions during its development. The work was supported by the MICINN with grant number DIN2019-010877. The authors greatly appreciate the support of by ESI Group on VAOne.

Appendix A. Vibro-acoustic modelling

Appendix A.1. Constitutive equations of orthotropic and isotropic solids

The equation of motion in an orthotropic solid of thickness L under plane stress conditions and with properties along the x_2 direction different from those in the (x_1, x_3) plane is

$$\nabla \boldsymbol{\sigma} = \rho \frac{\partial^2 \mathbf{u}}{\partial t^2}, \tag{A.1}$$

with $\boldsymbol{\sigma} = [\sigma_{11}\ \sigma_{22}\ \sigma_{12}]^{\mathrm{T}}$ being the stress tensor, $\mathbf{u} = [u_1\ u_2]^{\mathrm{T}}$ the displacement vector where $^{\mathrm{T}}$ is the transpose operator and ρ thef density of the solid. By considering the solid as a periodic repetition of a unit cell of length d_1 along the x_1 axis, the stress tensor and the displacement vector can

be written under the form of Bloch wave expansions

$$\sigma_{ij} = \sum_{\mu\in\mathbb{Z}} \sigma_{ij}^{\mu} e^{-\imath(k_1^{\mu}x_1 + k_2^{\mu}x_2)}, \tag{A.2}$$

$$u_i = \sum_{\mu\in\mathbb{Z}} u_i^{\mu} e^{-\imath(k_1^{\mu}x_1 + k_2^{\mu}x_2)}, \tag{A.3}$$

where $k_1^{\mu} = k_1 + (2\pi\mu/d_1)$, $k_2^{\mu} = \sqrt{k^2 - k_1^{\mu 2}}$, $k = \omega/c$ its wavenumber and $(i,j) \in \{1,2,3\}$. Introducing $\hat{\sigma}$ and $\hat{u}$ as the Space Fourier Transform of σ and u, Eq. (A.1) can be written, by considering harmonic displacements in the solid and by making use of the orthogonality property of the Space Fourier Transform, as

$$\begin{cases} -\imath k_1^{\mu}\hat{\sigma}_{11}^{\mu} + \dfrac{\partial\hat{\sigma}_{12}^{\mu}}{\partial x_2} = -\rho\omega^2\hat{u}_1^{\mu}, & \text{(A.4)} \\ -\imath k_1^{\mu}\hat{\sigma}_{12}^{\mu} + \dfrac{\partial\hat{\sigma}_{11}^{\mu}}{\partial x_2} = -\rho\omega^2\hat{u}_2^{\mu}. & \text{(A.5)} \end{cases}$$

The stress tensor $\boldsymbol{\sigma}$ is also related to the strain tensor ε of the solid by the generalised Hooke's law such that

$$\begin{bmatrix} \hat{\sigma}_{11}^{\mu} \\ \hat{\sigma}_{22}^{\mu} \\ \hat{\sigma}_{12}^{\mu} \end{bmatrix} = \mathbf{C} \begin{bmatrix} \hat{\varepsilon}_{11}^{\mu} \\ \hat{\varepsilon}_{22}^{\mu} \\ \hat{\varepsilon}_{12}^{\mu} \end{bmatrix}, \tag{A.6}$$

where $\mathbf{C}$ is the stiffness matrix whose terms depend only on the material properties of the solid and is expressed as:

$$\mathbf{C} = \begin{bmatrix} C_{11} & C_{12} & 0 \\ C_{21} & C_{22} & 0 \\ 0 & 0 & C_{33} \end{bmatrix}. \tag{A.7}$$

Note that Eq.(A.6) makes use of the symmetry property of the stress and strain tensors (i.e. $\hat{\sigma}_{12}^{\mu} = \hat{\sigma}_{21}^{\mu}$ and $\hat{\varepsilon}_{12}^{\mu} = \hat{\varepsilon}_{21}^{\mu}$. As a consequence, $\mathbf{C}$ is also symmetric ($C_{12} = C_{21}$). By using the relation between the deformations and the displacements in the solid $\hat{\varepsilon}_{mn} = \dfrac{1}{2}\left(\dfrac{\partial\hat{u}_m}{\partial x_n} + \dfrac{\partial\hat{u}_n}{\partial x_m}\right)$ in Eq.(A.6), and by applying the 2D Space Fourier Transform on the stress tensor and displacement vector, Eq.(A.6) becomes

$$\begin{cases} \hat{\sigma}_{11}^{\mu} = -\imath k_1^{\mu} C_{11}\hat{u}_1^{\mu} + C_{12}\dfrac{\partial\hat{u}_1^{\mu}}{\partial x_2}, & \text{(A.8)} \\ \hat{\sigma}_{22}^{\mu} = -\imath k_1^{\mu} C_{12}\hat{u}_1^{\mu} + C_{22}\dfrac{\partial\hat{u}_1^{\mu}}{\partial x_2}, & \text{(A.9)} \\ \hat{\sigma}_{12}^{\mu} = \dfrac{C_{33}}{2}\left(\dfrac{\partial\hat{u}_1^{\mu}}{\partial x_2} - \imath k_1^{\mu}\hat{u}_2^{\mu}\right). & \text{(A.10)} \end{cases}$$

Analogously, Eq.(A.1) can be written as

$$\begin{cases} -\imath k_1\hat{\sigma}_{11}^{\mu} + \dfrac{\partial\hat{\sigma}_{12}^{\mu}}{\partial x_2} = -\rho\omega^2\hat{u}_1^{\mu}, & \text{(A.11)} \\ -\imath k_1\hat{\sigma}_{12}^{\mu} + \dfrac{\partial\hat{\sigma}_{22}^{\mu}}{\partial x_2} = -\rho\omega^2\hat{u}_2^{\mu}. & \text{(A.12)} \end{cases}$$

In the case of isotropic materials, $\mathbf{C}$ becomes diagonal. As a result, Eqs. (A.8) - (A.10) remain the same except that $C_{12} = C_{21} = 0$.

Appendix A.2. Transfer Matrix Method

Appendix A.2.1. Case of a mono-layered solid

The wave propagation through the solid is studied by means of the Transfer Matrix Method (TMM). This method relies on the definition of a space dependent state vectors $\mathbf{W}^{\mu}$ for a given order μ of Bloch wave. $\mathbf{W}^{\mu}$ can be propagated along the x_2 direction by using a transfer matrix $\mathbf{M}^{\mu}$ that provides linear relations between the components of $\mathbf{W}^{\mu}$ at each fluid/solid interface (i.e. $x_2 = 0, L$) such that

$$\mathbf{W}^{\mu}(x_1, 0, \theta) = \mathbf{M}^{\mu}(\theta)\mathbf{W}^{\mu}(x_1, L, \theta). \tag{A.13}$$

In order to compute the sound reflection and transmission coefficients of the solid, the state vector is defined in this case as

$$\mathbf{W}^{\mu} = \begin{bmatrix} \sigma_{12}^{\mu} & \sigma_{22}^{\mu} & u_1^{\mu} & u_2^{\mu} \end{bmatrix}^{\mathrm{T}}. \tag{A.14}$$

The expression of $\mathbf{M}^{\mu}$ in Eq. (A.19) can be inferred from Stroh formalism, which presents the state vector as solution of a partial derivative equation at the first order. To obtain this equation, Eqs.(A.8) and (A.11) are first combined in order to suppress σ_{11}^{μ} such that

$$\frac{\partial\hat{\sigma}_{21}^{\mu}}{\partial x_2} - \imath k_1^{\mu} C_{12}\frac{\partial\hat{u}_2^{\mu}}{\partial x_2} + \left[\rho\omega^2 - C_{11}\left(k_1^{\mu}\right)^2\right]\hat{u}_1^{\mu} = 0. \tag{A.15}$$

Equation (A.9), (A.10), (A.12) and (A.15) can then be written in a matrix form as

$$\mathbf{B}^{\mu}\frac{\partial}{\partial x_2}\mathbf{W}^{\mu}+\mathbf{D}^{\mu}\mathbf{W}=\mathbf{0}, \tag{A.16}$$

with

$$\mathbf{B}^{\mu}=\begin{bmatrix}1 & 0 & 0 & -\imath k_1^{\mu}C_{12}\\ 0 & 1 & 0 & 0\\ 0 & 0 & C_{33}/2 & 0\\ 0 & 0 & 0 & C_{22}\end{bmatrix}, \tag{A.17}$$

$$\mathbf{D}^{\mu}=\begin{bmatrix}0 & 0 & \rho\omega^2-C_{11}\left(k_1^{\mu}\right)^2 & 0\\ -\imath k_1^{\mu} & 0 & 0 & \rho\omega^2\\ -1 & 0 & 0 & -\imath k_1^{\mu}C_{33}/2\\ 0 & -1 & -\imath k_1^{\mu}C_{12} & 0\end{bmatrix} \tag{A.18}$$

Equation (A.13) is solution of Eq. (A.16) with $\mathbf{M}^{\mu}(\theta)=e^{\mathbf{A}^{\mu}L}$ and $\mathbf{A}^{\mu}=\left(\mathbf{B}^{\mu}\right)^{-1}\mathbf{D}^{\mu}$.

Appendix A.3. Transfer Matrix of the multi-layered material

In the case of a multi-layered material made of two isotropic layers of composite material and an orthotropic honeycomb structure in-between, the total transfer matrix corresponds to the product of the transfer matrices of each layer such that

$$\mathbf{W}^{\mu}(x_1,0,\theta)=\mathbf{M}_T^{\mu}(\theta,\phi)\mathbf{W}^{\mu}(x_1,L,\theta). \tag{A.19}$$

where $\mathbf{M}_T^{\mu}=\mathbf{M}_c^{\mu}\mathbf{M}_h^{\mu}\mathbf{M}_c^{\mu}$ is the total transfer matrix of the sandwich solid and $\mathbf{M}_c^{\mu}$ and $\mathbf{M}_h^{\mu}$ are the transfer matrices of the composite layers and the honeycomb structure, respectively. $\mathbf{M}_c^{\mu}$ and $\mathbf{M}_h^{\mu}$ are computed by applying the procedure presented in Appendix A.2.1 for each layer taken independently.

Appendix A.3.1. Transfer matrix of the resonant layer

The analytical model used to define the transfer matrix of the resonant panel is well-known and is detailed in Refs. [33, 48]. This method relates the sound pressure p^m and the normal acoustic flow v^m on both sides of the resonant panel of length L_h such that

$$\begin{bmatrix}p^m\\ v^m\end{bmatrix}_{x=0}=\mathbf{T}\begin{bmatrix}p^m\\ v^m\end{bmatrix}_{x=L_h}, \tag{A.20}$$

where $\mathbf{T}=\mathbf{M}_{\Delta l_{slit}}\mathbf{M}_s\mathbf{M}_{HR}\mathbf{M}_s$. $\mathbf{M}_s$ is the transmission matrix through the slits of the panel and reads as

$$\mathbf{M}_s=\begin{bmatrix}\cos(k_s\frac{L_h}{2}) & iZ_s\sin(k_s\frac{L_h}{2})\\ \frac{i}{Z_s}\sin(k_s\frac{L_h}{2}) & \cos(k_s\frac{L_h}{2})\end{bmatrix}. \tag{A.21}$$

$\mathbf{M}_{HR}$ is the transmission matrix of the resonator such that

$$\mathbf{M}_{HR}=\begin{bmatrix}1 & 0\\ 1/Z_{HR} & 1\end{bmatrix}. \tag{A.22}$$

Finally the matrix $\mathbf{M}_{\Delta l_{slit}}$ represents the radiation correction of the slit to the free space and is expressed as

$$\mathbf{M}_{\Delta l_{slit}}=\begin{bmatrix}1 & Z_{\Delta l_{slit}}\\ 0 & 1\end{bmatrix}, \tag{A.23}$$

where $Z_{\Delta l_{slit}}=-i\omega\Delta l_{slit}\rho/\phi_t S_0$ is the characteristic radiation impedance with Δl_{slit} the end correction.

Appendix A.4. Scattering problem with a layered material

Considering the problem depicted in Fig. 3b, the pressure field on both sides of the system can be expressed in the frequency domain as a Bloch wave decomposition of the field such that

$$p^0=\sum_{\mu\in\mathbb{Z}}\left(\delta_{\mu 0}e^{-\imath k_2^{\mu}x_2}+R_{\mu}^{S}(\theta)e^{\imath k_2^{\mu}x_2}\right)e^{-\imath k_1^{\mu}x_1},\qquad x_2\leq 0, \tag{A.24}$$

$$p^{L_s+L_h}=\sum_{\mu\in\mathbb{Z}}T_{\mu}^{F}(\theta)e^{\imath k_2^{\mu}(x_2-L_s-L_h)}e^{-\imath k_1^{\mu}x_1},\qquad x_2\geq L_s+L_h, \tag{A.25}$$

where $L_s=h^{s_1}+2h^{s_2}$, and R_{μ}^{S} and T_{μ}^{F} are the reflection and transmission coefficients of the sandwich panel and the resonant panel, respectively. The pressure field at the interface between both panels also reads as

$$p^{L_h}=\sum_{\mu\in\mathbb{Z}}\left[R_{\mu}^{F}(\theta)+T_{\mu}^{S}(\theta)\right]e^{-\imath k_1^{\mu}x_1},\qquad x_2=L_s, \tag{A.26}$$

where R_μ^F and T_μ^S are the reflection and transmission coefficients of the resonant panel and the sandwich panel, respectively. The continuity of normal stresses and velocities between the sandwich panel, the resonant panel and the air fluid read as

$$\hat{\sigma}_{12}^\mu(0,\theta) = \hat{\sigma}_{12}^\mu(L_s,\theta) = 0, \tag{A.27}$$
$$\hat{\sigma}_2^\mu(0,\theta) = -(\delta_{\mu 0} + R_\mu^S(\theta)), \tag{A.28}$$
$$\hat{\sigma}_2^\mu(L_h,\theta) = -(T_\mu^S + R_\mu^F)(\theta), \tag{A.29}$$
$$\hat{v}_{2,\mu}^s(0,\theta) = \hat{v}_{2,\mu}^f(0,\theta), \tag{A.30}$$
$$\hat{v}_{2,\mu}^s(L_s,\theta) = \hat{v}_{2,\mu}^f(L_s,\theta). \tag{A.31}$$

where $\hat{v}_{2,\mu}^s$ and $\hat{v}_{2,\mu}^f$ are the normal velocities in the sandwich and resonant panels, respectively. In particular, $\hat{v}_{2,\mu}^s$ and $\hat{v}_{2,\mu}^f$ can be expressed according to the normal displacement $\hat{u}_2^\mu$ of the solid and the acoustic pressure, respectively. Therefore, the two last equations become

$$\hat{u}_2^\mu(0,\theta) = \frac{-\imath k_2^\mu}{\omega^2\rho}(1 - R_\mu^S(\theta)), \tag{A.32}$$
$$\hat{u}_2^\mu(L_h,\theta) = \frac{-\imath k_2^\mu}{\omega^2\rho}(T_\mu^S(\theta) - R_\mu^F(\theta)(\theta)). \tag{A.33}$$

The state vector can therefore be written at both fluid-solid interfaces as,

$$\mathbf{W}^\mu(0,\theta) = \mathbf{S}^\mu + \mathbf{L}_0^\mu \begin{bmatrix} \hat{u}_1^\mu(0,\theta) \\ \hat{u}_1^\mu(L_s,\theta) \\ R_\mu^S(\theta) \\ T_\mu^S(\theta) \\ R_\mu^F(\theta) \end{bmatrix}, \tag{A.34}$$

$$\mathbf{W}^\mu(L_h,\theta) = \mathbf{L}_{L_s}^\mu \begin{bmatrix} \hat{u}_1^\mu(0,\theta) \\ \hat{u}_1^\mu(L_s,\theta) \\ R_\mu^S(\theta) \\ T_\mu^S(\theta) \\ R_\mu^F(\theta) \end{bmatrix}, \tag{A.35}$$

with

$$\mathbf{S}^\mu = \begin{bmatrix} 0 \\ -\delta_{\mu 0} \\ 0 \\ \frac{-\imath k_2^\mu \delta_{\mu 0}}{\omega^2\rho} \end{bmatrix}, \tag{A.36}$$

$$\mathbf{L}_0^\mu = \begin{bmatrix} 0 & 0 & 0 & 0 & 0 \\ 0 & 0 & -1 & 0 & 0 \\ 1 & 0 & 0 & 0 & 0 \\ 0 & 0 & \frac{\imath k_2^\mu}{\omega^2\rho} & 0 & 0 \end{bmatrix}, \tag{A.37}$$

$$\mathbf{L}_{L_h}^\mu = \begin{bmatrix} 0 & 0 & 0 & 0 & 0 \\ 0 & 0 & 0 & -1 & -1 \\ 0 & 1 & 0 & 0 & 0 \\ 0 & 0 & 0 & \frac{-\imath k_2^\mu}{\omega^2\rho} & \frac{\imath k_2}{\omega^2\rho} \end{bmatrix}. \tag{A.38}$$

Equation (A.15) can then be rewritten as

$$(\mathbf{M}_{wall}^\mu \mathbf{L}_{L_s}^\mu - \mathbf{L}_0^\mu) \begin{bmatrix} \hat{u}_1^\mu(0,\theta) \\ \hat{u}_1^\mu(L_s,\theta) \\ R_\mu^S(\theta) \\ T_\mu^S(\theta) \\ R_\mu^F(\theta) \end{bmatrix} = \mathbf{S}^\mu. \tag{A.39}$$

This represents a system with 5 unknowns and 4 equations and cannot be solved as is. To do that, we have to apply the boundary conditions at $x_2 = L_s$ and $x_2 = L_s + L_h$ can be written by considering pressures and normal velocities continuity at both ends of each slit of the resonant panel. Since the normal mode of the slits along x_1 is only considered here, the boundary conditions at $x_2 = L_s$ and $x_2 = L_s + L_h$ can be written as

$$\sum_{\mu\in\mathbb{Z}} (T_\mu^S + R_\mu^H) I_\mu^- = \hat{p}^m(L_s) h_s, \tag{A.40}$$
$$\frac{d_1 k_2^\nu}{\rho\omega}(T_\nu^S - R_\nu^H) = \hat{v}^m(L_s) I_\nu^+ \tag{A.41}$$
$$\sum_{\mu\in\mathbb{Z}} T_\mu^H I_\mu^- = \hat{p}^m(L_s + L_h) h_s, \tag{A.42}$$
$$\frac{d_1 k_2^\nu}{\rho\omega} T_\nu^H = \hat{v}^m(L_s + L_h) I_\nu^+, \tag{A.43}$$

where,

$$I_\nu^\pm = \int_0^{h_s} e^{\pm\imath k_1^\nu x_1} dx_1 = h_s \mathrm{sinc}(k_1^\nu \frac{h_s}{2}) e^{\pm\imath k_1^\nu/2}. \tag{A.44}$$

Now applying the transfer matrix method of the resonant layer, described in Appendix A.3.1, we have:

$$\sum_{\mu\in\mathbb{Z}} (T_\mu^S + R_\mu^H) I_\mu^- = \hat{p}^m(L_s) h_s, \tag{A.45}$$

$$\frac{d_1 k_2^\nu}{\rho\omega}(T_\nu^S - R_\nu^H) = \hat{v}^m(L_s) I_\nu^+ \tag{A.46}$$

$$\sum_{\mu\in\mathbb{Z}} T_\mu^H I_\mu^- = \left(T_{11}^m \hat{p}^m(L_s) + S_s T_{12}^m \hat{v}^m(L_s)\right) h_s, \tag{A.47}$$

$$\frac{d_1 k_2^\nu}{\rho\omega} T_\nu^H = \left(\frac{T_{21}^m}{S_s}\hat{p}^m(L_s) + T_{22}^m \hat{v}^m(L_s)\right) I_\nu^+, \tag{A.48}$$

where $S_s = d_1 h_3$ is the cross-sectional area. Finally, by substituting the expressions of $\hat{p}^m(L_s)$ from Eq. (A.45) and $\hat{v}^m(L_s)$ from Eq. (A.46) in the two last equations Eqs. (A.47) and (A.48) we obtain

$$T_{11}^m \sum_{\mu\in\mathbb{Z}} (T_\mu^S + R_\mu^H) I_\mu^- + \frac{k_2^\mu Q_1}{I_\mu^+}(T_\nu^S - R_\nu^H) - \sum_{\mu\in\mathbb{Z}} T_\mu^H I_\mu^- = 0, \tag{A.49}$$

$$I_\nu^+ \frac{T_{21}^m}{S_s h_s} \sum_{\mu\in\mathbb{Z}} (T_\mu^S + R_\mu^H) I_\mu^+ + k_2^\mu Q_2 (T_\nu^S - R_\nu^H) - \frac{k_2^\mu d_1}{\rho\omega} T_\nu^H = 0, \tag{A.50}$$

where $Q_1 = \frac{h_s S_s d_1 T_{11}^m}{\rho\omega}$ and $Q_2 = \frac{T_{22}^m S_s^{in} d_1}{S_s^{out}\rho\omega}$. This equation system is not sufficient to compute the scattering coefficients R_μ^S, T_μ^S, R_μ^H and T_μ^H can then been computed by solving the equations system composed of Eqs. (A.49) , (A.50) and A.39. Once the complete system is solved, it is possible to compute the R^S, T^S, R^H and T^H as follows

$$|R|^2 = \sum_{\mu\in\mathbb{Z}} \frac{\mathrm{Re}(k_2^\mu)}{k_2^0} |R_\mu^S|^2, \tag{A.51}$$

and

$$|T|^2 = \sum_{\mu\in\mathbb{Z}} \frac{\mathrm{Re}(k_2^\mu)}{k_2^0} |T_\mu^H|^2. \tag{A.52}$$

References

[1] G. Denis, D. Alary, X. Pasco, N. Pisot, D. Texier, S. Toulza, From new space to big space: How commercial space dream is becoming a reality, Acta Astronautica 166 (2020).

[2] ECSS, Spacecraft mechanical loads analysis handbook, European Cooperation for Space Standardization (2013).

[3] J. P. Arenas, R. N. Margasahayam, Ingeniare. Revista chilena de ingeniería 14 (3) (dec 2006).

[4] R. Camussi, A. Di Marco, C. Stoica, M. Bernardini, F. Stella, F. De Gregorio, F. Paglia, L. Romano, D. Barbagallo, Wind tunnel measurements of the surface pressure fluctuations on the new vega-c space launcher, Aerospace Science and Technology 99 (2020) 105772. doi:https://doi.org/10.1016/j.ast.2020.105772.

[5] arianespace, VEGA User's manual, issue 4 revision 0 Edition (April 2014).

[6] C. Jiang, T. Han, Z. Gao, C. H. Lee, A review of impinging jets during rocket launching (8 2019). doi:https://doi.org/10.1016/j.paerosci.2019.05.007.

[7] J. J. Wijker, Random vibrations in spacecraft structures design: theory and applications, Vol. 165, Springer Science & Business Media, 2009.

[8] H. H. Hubbard, Aeroacoustics of flight vehicles: Theory and practice. Volume 1. Noise sources., Ntional Aeronautics and Space Admin Langley Research Center Hampton Va, 1991.

[9] S. Frikha, M. A. Hamdi, P. Roux, L. Mebarek, Noise reduction prediction of ariane 5 fairing with acoustic protection made of porous-elastic material, Journal of the Acoustical Society of America (2008).

[10] A. C. Abeel, E. M. Wooldridge, M. Calcabrini, J. O. Ward, O. Schmeitzky, Overview of contamination control for the james webb space telescope launch campaign, in: Space Systems Contamination: Prediction, Control, and Performance 2022, Vol. 12224, SPIE, 2022.

[11] S. J. Esteve, Control of sound transmission into payloadfairings using distributed vibration absorbersand helmholtz resonators, Ph.D. thesis (2004).

[12] S. A. Lane, S. Kennedy, R. Richard, Noise Transmission Studies of an Advanced Grid-Stiffened Composite Fairing (5) 1131–1139. doi:https://doi.org/10.2514/1.28590.

[13] S.-H. Park, S.-H. Seo, H.-K. Jeong, Y.-S. Jang, Y.-M. Yi, G.-R. Cho, Lift-off vibro-acoustic analysis of the upper stage of small launch vehicle, in: 13th International Congress on Sound and Vibration 2006, ICSV 2006, Vol. 7, pp. 5900–5907.

[14] A. Cherian, P. George, C. Prabha, Response Analysis Of Payload Fairing Due To Acoustic Excitation.

[15] S.-H. Park, A design method of micro-perforated panel absorber at high sound pressure environment in launcher fairings (3) 521–535. doi:https://doi.org/10.1016/j.jsv.2012.09.015.

[16] Modeling of perforated plates and screens using rigid frame porous models, Journal of Sound and Vibration 303 (1) (2007) 195–208. doi:https://doi.org/10.1016/j.jsv.2007.01.012.

[17] A. Sanchez-Cebrian, S. Freiburghaus, D. Tonon, U. Pachale, S. Schoenwald, T. Gerngross, Development of an enhanced fairing acoustic protection system to increase payload comfort, in: 8th European Conference for Aeronautics and Space Sciences (EUCASS).
URL www.eucass.eu/doi/EUCASS2019-0747.pdf

[18] Atlas launch system mission planner's guide.

[19] S.-H. Seo, H.-K. Jeong, S.-H. Park, Y.-S. Jang, Y.-M. Yi, G.-R. Cho, Sound reduction by using acoustic resonators for payload fairing of small launch vehicle, in: 14th International Congress on Sound and Vibration 2007, ICSV 2007, Vol. 3, pp. 2197–2203.

[20] S. Unnikrishnan Nair, C. D. Shete, A. Subramoniam, K. L. Handoo, C. Padmanabhan, Experimental and computational investigation of coupled resonator–cavity systems (1) 61–67. doi:https://doi.org/10.1016/j.apacoust.2009.07.009.

[21] S. A. Lane, R. E. Richard, S. J. Kennedy, Fairing Noise Control Using Tube-Shaped Resonators (4) 640–646. doi:https://doi.org/10.2514/1.7816.

[22] D. Li, J. S. Vipperman, Noise Control of Mock-Scale ChamberCore Payload Fairing Using Integrated Acoustic Resonators (4) 877–882. doi:https://doi.org/10.2514/1.16331.

[23] B. N. Rosenthal, J. W. Herlan, A. R. Allen, N. H. Schiller, Experimental Evaluation of Tuned Chamber Core Panels for Payload Fairing Noise Control, in: 29th Aerospace Testing Seminar.

[24] E. Ardelean, A. Williams, N. Korshin, K. Henderson, S. Lane, R. Richard, Chamber-core structures for fairing acoustic mitigation, in: Smart Structures and Materials 2005: Damping and Isolation, Vol. 5760, SPIE, pp. 361–369. doi:https://doi.org/10.1117/12.600125.

[25] S. A. Lane, K. Henderson, A. Williams, E. Ardelean, Chamber Core Structures for Fairing Acoustic Mitigation (1) 156–163. doi:https://doi.org/10.2514/1.17673.

[26] B. Ahn, S. Lee, Integrated Acoustic Analysis of Payload Fairing Using an FE-SEA Hybrid Method (1) 1–8. doi:https://doi.org/10.1007/s42405-022-00500-4.

[27] S. Griffin, S. A. Lane, C. Hansen, B. Cazzolato, Active Structural-Acoustic Control of a Rocket Fairing Using Proof-Mass Actuators (2) 219–225. doi:https://doi.org/10.2514/2.3673.

[28] S. A. Lane, M. Johnson, C. Fuller, A. Charpentier, Active control of payload fairing noise (3) 794 – 819. doi:https://doi.org/10.1016/j.jsv.2005.04.017.

[29] J. D. Kemp, R. L. Clark, Noise reduction in a launch vehicle fairing using actively tuned loudspeakers (4) 1986–1994. doi:https://doi.org/10.1121/1.1558371.

[30] A. Merkel, G. Theocharis, O. Richoux, V. Romero-García, V. Pagneux, Control of acoustic absorption in one-dimensional scattering by resonant scatterers, Appl. Phys. Lett. (24) 244102. arXiv:https://doi.org/10.1063/1.4938121, doi:https://doi.org/10.1063/1.4938121.

[31] V. Romero-García, G. Theocharis, O. Richoux, A. Merkel, V. Tournat, V. Pagneux, Perfect and broadband acoustic absorption by critically coupled sub-wavelength resonators 6 (1). doi:https://doi.org/10.1038/srep19519.

[32] V. Romero-García, N. Jiménez, G. Theocharis, V. Achilleos, A. Merkel, O. Richoux, V. Tournat, J.-P. Groby, V. Pagneux, Design of acoustic metamaterials made of Helmholtz resonators for perfect absorption by using the complex frequency plane, Comptes Rendus. Physique 21 (7-8) (2020) 713–749. doi:https://doi.org/10.5802/crphys.32.

[33] V. Romero-García, A. Hladky-Hennion, Fundamentals and Applications of Acoustic Metamaterials: From Seismic to Radio Frequency, ISTE Willey, 2019.

[34] J. Boulvert, T. Humbert, V. Romero-García, G. Gabard, E. R. Fotsing, A. Ross, J. Mardjono, J.-P. Groby, Perfect, broadband, and subwavelength absorption with asymmetric absorbers: Realization for duct acoustics with 3d printed porous resonators, Journal of Sound and Vibration 116687doi:https://doi.org/10.1016/j.jsv.2021.116687.

[35] Y. Meng, V. Romero-García, G. Gabard, J.-P. Groby, C. Bricault, S. Goudé-doi:https://doi.org/10.1002/admt.202201909.

[36] V. Romero-García, N. Jiménez, J.-P. Groby, A. Merkel, V. Tournat, G. Theocharis, O. Richoux, V. Pagneux, Perfect absorption in mirror-symmetric acoustic metascreens, Phys. Rev. Applied 14 (054055) (2020).

[37] M. Yang, C. Meng, C. Fu, Y. Li, Z. Yang, P. Sheng, Subwavelength total acoustic absorption with degenerate resonators, Appl. Phys. Lett. 107 (10) (2015) 104104.

[38] Fundamentals and Applications of Acoustic Metamaterials: From Seismic to Radio Frequency, Wiley.

[39] N. Jiménez, J.-P. Groby, V. Romero-García, The Transfer Matrix Method in Acoustics: Modelling One-Dimensional Acoustic Systems, Phononic Crystals and Acoustic Metamaterials, Springer International Publishing, pp. 103–164.

[40] N. Jiménez, W. Huang, V. Romero-García, V. Pagneux, J.-P. Groby, Ultra-thin metamaterial for perfect and quasi-omnidirectional sound absorption, Appl. Phys. Lett. (12) 121902. arXiv:https://doi.org/10.1063/1.4962328, doi:10.1063/1.4962328.

[41] M. R. Stinson, The propagation of plane sound waves in narrow and wide circular tubes, and generalization to uniform tubes of arbitrary cross-sectional shape 89 (2) 550–558. doi:https://doi.org/10.1121/1.400379.

[42] M. J. D. Powell, A fast algorithm for nonlinearly constrained optimization calculations, in: Lecture Notes in Mathematics, Springer Berlin Heidelberg, pp. 144–

157. doi:https://doi.org/10.1007/bfb0067703.
[43] Mathworks, Matlab.
URL http://matlab.mathworks.com
[44] T. J. Hughes, The finite element method: linear static and dynamic finite element analysis, Courier Corporation, 2012.
[45] C. A. Brebbia, J. C. F. Telles, L. C. Wrobel, Boundary element techniques: theory and applications in engineering, Springer Science & Business Media, 2012.
[46] ESI Group, Vaone.
URL https://www.esi-group.com
[47] M. S. Escartí-Guillem, P. Barriuso Feijoo, A. Cebrecos, M. Chimeno Manguán, P. Cobo, L. M. García-Raffi, J. Groby, H. Philippe, J. Sergio, L. Noé, et al., Application of metamaterials to control noise scattering during space vehicle lift-off, Euronoise, 2021.
[48] N. Jiménez, O. Umnova, J.-P. Groby (Eds.), Acoustic Waves in Periodic Structures, Metamaterials, and Porous Media, Springer International Publishing, Cham, Switzerland. doi:https://doi.org/10.1007/978-3-030-84300-7.